

Effect of Nozzle Type on the Performance of Bubble Augmented Waterjet Propulsion

Xiongjun Wu¹, Jin-Keun Choi², Abigail Leaman Nye³, and Georges L. Chahine⁴

^{1,2,3,4}DYNAFLOW INC.

10621-J Iron Bridge Road, Jessup, MD 20794, USA

www.dynaflo.com

ABSTRACT

Injection of bubbles in a waterjet can significantly augment thrust especially at high bubble volume fractions. A convergent-divergent nozzle could potentially enhance thrust further if choked flow conditions can be achieved. To investigate this potential, two types of nozzles were studied: a divergent-convergent configuration and a convergent-divergent configuration. Investigations included flow visualization, particle image velocimetry, and pressure measurements for different air volume fractions. The convergent-divergent nozzle exhibited at high void fractions some of the anticipated characteristics of supersonic flow; i.e. reversal of pressure and velocity gradients after the throat. It also achieved better thrust augmentation performance than the divergent-convergent nozzle. However, direct observation of a shock in the nozzle remained elusive.

Keywords

Bubbly flow, Waterjet, Thrust, Choked flow.

1 INTRODUCTION

Augmentation of waterjet thrust through bubble injection has been a subject of interest for many years with the aim to improve jet propulsion net thrust, particularly for planing or semi-planing ships with hump speeds. Unlike traditional propulsion devices which are typically limited to less than 50 knots, the bubble augmented propulsion concept is thought to promise thrust augmentation even at very high vehicle speeds (Mor and Gany 2004).

Recent efforts have demonstrated that bubble injection can significantly improve the net thrust of a water jet (Chahine, Hsiao, Choi, & Wu, 2008; Wu, Choi, Hsiao, & Chahine, 2010; Gany & Gofer, 2011; Wu, Choi, Singh, Hsiao, &

Chahine, 2012; Wu, Singh, Choi, & Chahine, 2012). In addition, extensive analytical, numerical, and experimental research of bubble flow effects has focused on the effects of geometry on multiphase flow properties and structures in pipes and nozzles (Tangren, Dodge, & Seifert, 1949; Muir & Eichhorn, 1963; Ishii, Umeda, Murata, & Shishido, 1993; Kameda & Matsumoto, 1995; Wang & Brennen, 1999; Aloui, Doublier, Legrand, & Souhar, 1999; Preston, Colonius, & Brennen, 2000; Bertola, 2004; Ahmed, Ching, & Shoukri, 2007; Kourakos, Rambaud, Chabane, Pierrat, & Buchlin, 2009; Balakhrisna, Ghosh, Das, & Das, 2010; Eskin & Deniz, 2012).

Figure 1 illustrates the concept for a divergent-convergent nozzle. Gas is injected via mixing ports in the high pressure region following the divergent section. The resulting multiphase mixture is then accelerated in the convergent section of the nozzle, where the injected bubbles increase in volume due to the pressure drop. This bubble presence and growth converts potential energy associated with the bubbles into liquid kinetic energy and increases momentum of the jet at the exit and therefore boosts the jet thrust.

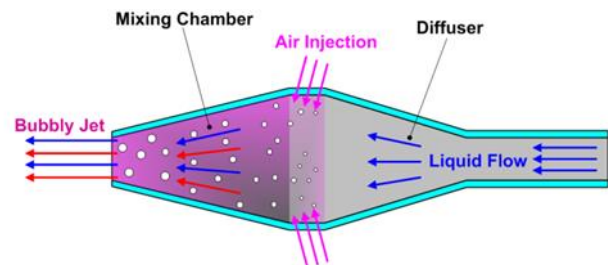


Figure 1: Concept sketch of bubble augmented jet propulsion.

It is well established that the speed of sound in the bubbly mixture decreases substantially with increased void fraction

and can reach values as low as 20 m/s (Brennen, 1995). On the other hand, for the same incoming liquid velocity, the mixture velocity increases with the void fraction. Therefore, conditions can be realized where the local mixture velocity exceeds the speed of sound, resulting in supersonic choked flow conditions in the throat region of a convergent-divergent nozzle. Fundamental two-phase flow studies (e.g. Mor & Gany, 2004; Singh, Fourmeau, Choi, & Chahine, 2014) have shown that higher thrusts could be achieved if a choked flow condition could be realized within the nozzle.

In this paper, we present experimental and numerical results for the two types of nozzles and discuss geometry effects on nozzle performance.

2 NUMERICAL METHODS

2.1 Governing Equations

A continuum homogeneous model of a bubbly mixture satisfies the following continuity and momentum equations:

$$\begin{aligned} \frac{\partial \rho_m}{\partial t} + \nabla \cdot (\rho_m \mathbf{u}_m) &= 0, \\ \rho_m \frac{D\mathbf{u}_m}{Dt} &= -\nabla p_m + \nabla \cdot \left\{ 2\mu_m \delta_{ij} - \frac{2}{3}\mu_m (\nabla \cdot \mathbf{u}_m) \right\}, \end{aligned} \quad (1)$$

where ρ_m , \mathbf{u}_m , p_m are the mixture density, velocity and pressure respectively, the subscript m represents the mixture medium, and δ_{ij} is the Kronecker delta.

The mixture density and the mixture viscosity can be expressed as

$$\rho_m = (1-\alpha)\rho_\ell + \alpha\rho_g, \quad (2)$$

$$\mu_m = (1-\alpha)\mu_\ell + \alpha\mu_g, \quad (3)$$

where α is the local void fraction, defined as the local volume occupied by the bubbles per unit mixture volume. The subscript ℓ represents the liquid and the subscript g represents the bubbles. The continuum flow field has a space and time dependent density, similar to a compressible liquid problem.

Bubble dynamics are solved using the Keller-Herring equation that includes the effect of the surrounding medium compressibility with a Surface-Averaged Pressure (SAP) scheme (G. L. Chahine, 2008). Bubble trajectories are obtained from a bubble motion equation similar to that derived by (Johnson & Hsieh, 1966), as described in (Wu, Choi, et al., 2012), which incorporates drag, added mass

variation, pressure gradient within the medium, buoyancy, and shear generated lift (Saffman, 1965; Li & Ahmadi, 1992) forces acting on the bubble.

2.2 Simple One-Dimensional Modelling

To study conditions where the flow can be considered one-dimensional with cross-section averaged quantities, a 1D steady state version of the above approach was developed and used (G. Chahine et al., 2008; S. Singh, Choi, & Chahine, 2012), especially for design studies as described in (Wu, Choi, et al., 2012; Wu, Singh, et al., 2012). The governing equations for unsteady 1D flow through a nozzle of varying cross-section, $A(x)$, can be reduced to a simplified form that depends only on $A(x)$. In this formulation, the liquid is assumed incompressible and the dispersed gas phase is responsible for all the compressibility effects of the mixture. It is also assumed that no bubbles are created or destroyed other than at the injection location.

2.3 3D Unsteady Fully Coupled Modeling

The 3D coupling between the mixture flow field and the bubble dynamics and tracking is realized by coupling the viscous Eulerian code, 3DYNAPS_Vis[®], with the Lagrangian multi-bubble dynamics code 3DYNAPS_DSM[®]. The unsteady two-way interaction can be described as follows. The dynamics of the bubbles in the flow field are determined by the local densities, velocities, pressures, and pressure gradients of the mixture medium. The mixture flow field is influenced by the presence of the bubbles. The local void fraction, and accordingly the local mixture density, is modified by the migration and size change of the bubbles, i.e., the bubble number density and sizes. The flow field is adjusted according to the modified mixture density distribution in such a way that the continuity and momentum are conserved through equations (1) to (3).

The two-way interaction described above is very strong as the void fraction can change significantly (from near zero in the water inlet to as high as 70% at the nozzle exit) in Bubble Augmented jet Propulsion (BAP) applications.

3 THRUST AUGMENTATION PARAMETERS

The thrust can be defined in two different ways, depending on whether the nozzle application type is classified as ‘ramjet’ or ‘waterjet’ (G. Chahine et al., 2008; Wu et al., 2010). Ramjet thrust, T_R , and waterjet thrust, T_W , are computed as follows using an integration control surface, \mathcal{A} , that encompasses both the inlet and the outlet areas of the

ramjet nozzle and an integration control surface that encompasses the outlet surface area, \mathcal{A}_o , of the waterjet nozzle respectively:

$$T_R = \iint_{\mathcal{A}} (p + \rho_m u_m^2) d\mathcal{A}, \quad (4)$$

$$T_W = \iint_{\mathcal{A}_o} \rho_m u_m^2 d\mathcal{A}. \quad (5)$$

where u_m is the axial component of the mixture velocity. For ramjet propulsion, the force due to pressure and momentum over both the inlet and outlet of the nozzle need to be included. For a waterjet nozzle, only the thrust due to the exit water jet momentum is of interest.

Under the 1D assumption, these thrusts can be simplified to:

$$T_R = (p_o \mathcal{A}_o - p_i \mathcal{A}_i) + (\rho_{m,o} \mathcal{A}_o u_{m,o}^2 - \rho_{m,i} \mathcal{A}_i u_{m,i}^2), \quad (6)$$

$$T_W = \rho_{m,o} \mathcal{A}_o u_{m,o}^2,$$

where \mathcal{A}_i and $u_{m,i}$ are respectively the inlet area and average velocity at the inlet.

To evaluate the performance of a nozzle design with air injection, we define a normalized relative thrust augmentation parameter, ξ , as the following:

$$\xi_i = \frac{T_{i,\alpha} - T_i}{T_i}, \quad i = R \text{ or } W, \quad (7)$$

in which $T_{i,\alpha}$ and T_i are thrusts with and without bubble injection.

We can also define a normalized momentum thrust augmentation parameter, ξ_m , as the net thrust increase with bubble injection normalized by the inlet momentum flux, $T_{m-inlet} = \rho A u^2|_{inlet}$, as the following:

$$\xi_m = \frac{T_{i,\alpha} - T_i}{T_{m-inlet}} \quad i = R \text{ or } W \quad (8)$$

4 NOZZLE DESIGN AND OPTIMIZATION

4.1 Divergent-Convergent Nozzle

A series of numerical studies was previously conducted to study the effects of nozzle geometry on the thrust augmentation (Wu et al., 2010; S. Singh et al., 2012). For a divergent-convergent nozzle, an important design parameter

is the ratio of the exit area to the inlet area or the ‘contraction ratio’ defined as

$$C = \mathcal{A}_o / \mathcal{A}_i. \quad (9)$$

In order to obtain thrust augmentation, C should be larger than 0.6 (S. Singh et al., 2012). In addition, it was demonstrated that there $C \sim 1.0$ was an optimal value for different bubble injection void fractions (Wu et al., 2010). The simulation results also indicated that for a given nozzle inlet area, the net thrust increase is dominantly controlled by the exit area, with little change in thrust observed for variations in nozzle length and cross-section (Wu, Singh, et al., 2012). In particular, it was shown that for divergent-convergent nozzle designs, the variation of the nozzle cross-section has negligible influence on the nozzle thrust performance.

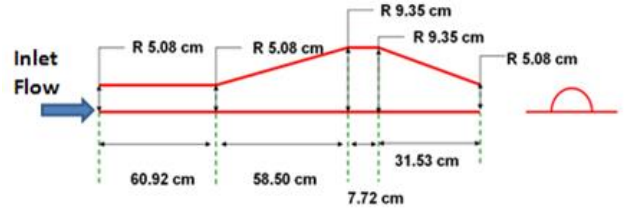


Figure 2: Dimensions of the half 3D nozzle designed and built for optimal thrust augmentation.

Based on these numerical simulations, a nozzle with equal inlet and exit areas was designed and built. Figure 2 shows the dimensions of the nozzle used in the experimental study presented below. As shown in the figure, a ‘half’ version of the three dimensional nozzle was used, which was created from the full three dimensional axisymmetric nozzle design by taking a bisecting vertical cut along the nozzle in a longitudinal plane aligned with the direction of flow. The transparent center-plane wall of the bisected nozzle enables improved flow visualization as compared with visualizations through the curved and varying thickness walls of the full three dimensional axisymmetric nozzle.

4.2 Convergent- Divergent Nozzle

In comparison with a divergent-convergent nozzle, a convergent-divergent nozzle has the potential to significantly boost the nozzle performance by generating a mixture flow that chokes at the throat region and achieves supersonic flow in the divergent exit section. In order to design and optimize a convergent-divergent nozzle, the analytical expressions for choked flows in nozzles (Brennen, 1995) were used in the simulations. The results depend only on the ratios of the cross-sectional areas of the throat over the inlet section, $\mathcal{A}_{throat}/\mathcal{A}_i$, and that of the exit

area over the inlet area, A_0/A_i (Sowmitra Singh et al., 2014). With this tool in hand, systematic simulations can be conducted to search for the optimal nozzle design that can maximize ξ_m by varying the contraction ratios: A_{throat}/A_i and A_0/A_i for a given inlet pressure and injection area over inlet area ratio.

Considering the above as well as the limits of the pumps in our facilities (described later), we aimed for an inlet velocity of about 25 m/s, an inlet pressure of about 300 kPa (44 psi), and injection void fractions in the 50% range. We aimed at achieving a ξ_m of about 1.0 with the new choked flow nozzle, which is more than twice the value of $\xi_m \sim 0.45$ that we had achieved previously with the subsonic mixture flow nozzles.

Figure 3 shows a drawing of the design. Two nozzles based on this design were fabricated: (a) an axisymmetric version, and (b) a square version. A picture of the completed axisymmetric nozzle is shown in Figure 4. Pressure ports are arranged along the nozzle for pressure measurement. This nozzle was used to measure the pressure profile along the nozzle and to evaluate the thrust augmentation performance. Without the optical distortion imposed by the curved and varying thickness walls of the axisymmetric version, this square nozzle can provide much better optical access. Therefore this nozzle was used for flow visualization and PIV measurements to better understand the mixture flow inside the nozzle.

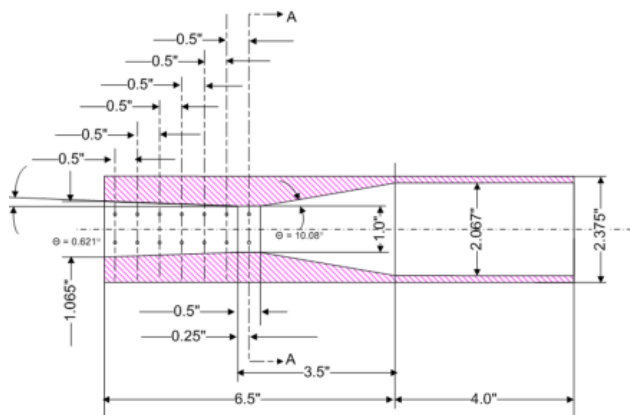


Figure 3: Design of the convergent-divergent nozzle with the flow direction from right to left.

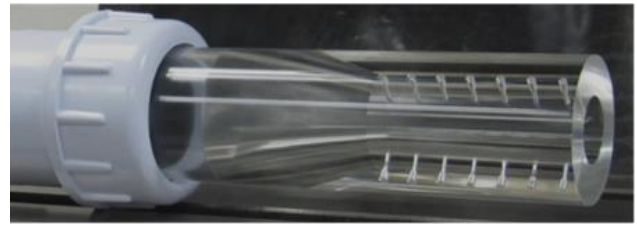


Figure 4: A picture of the axisymmetric version of the nozzle shown in Figure 3 with pressure measurement ports distributed along the nozzle. Flow direction is from left to right.

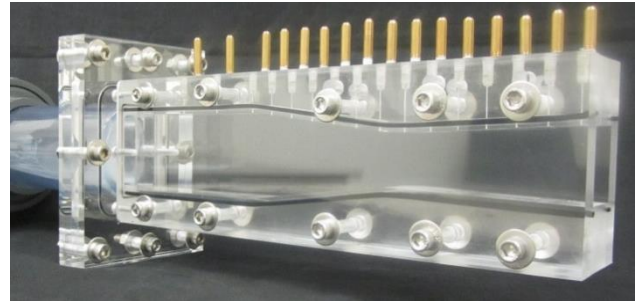


Figure 5: A picture of the square version of the nozzle shown in Figure 3 with pressure measurement ports distributed along the nozzle. Flow direction is from left to right.

5 EXPERIMENTAL SETUP

5.1 Facility

The test setup used in this study is shown in

Figure 6. Two 15 HP pumps (Goulds Model 3656) can be used to deliver the liquid flow. Each pump capable of a flow rate of 2.16 m³/min (570 gpm) at 180 kPa (26 psi) or 1.21 m³/min (320 gpm) at 410 kPa (60 psi). In this study, the two pumps were used simultaneously in a series configuration in order to increase the upstream pressure and thereby achieve high void fraction flows in experiments.

The pumps are hooked up to the DYNAFLOW wind wave tank, which is used here as a very large water reservoir, so that accumulation of air bubbles in the liquid flow input is minimized. For the half-3D divergent-convergent nozzle and the square convergent-divergent nozzle, a flow adaptor was used to convert the flow from the upstream circular cross-section to match the cross-section shape of the nozzle assembly geometry. For the half-3D divergent-convergent nozzle, a flow straightening section was also inserted between the flow adaptor and the nozzle inlet.

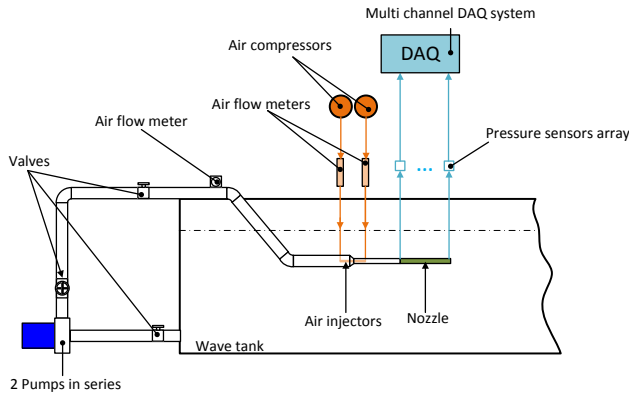


Figure 6: Sketch of the test setup for the Bubble Augmented Propulsion experiment.

In order to achieve a bubble distribution as uniform as possible, air injectors made from a flexible porous membrane that conforms to the nozzle inner shape were used for the half-3D divergent-convergent nozzle. Figure 7 and Figure 8 shows the arrangement of the inner and outer injectors. For the convergent-divergent nozzles, air injection was achieved through a bundle of six 24-inch microporous tubes with 10 μm average pore size placed along the axis of the piping system upstream of the nozzles, Figure 9 shows a sketch of the injection scheme.

To supply enough air flow for high void fraction injection, two high capacity air compressors were used. These 5 hp air compressors (Compbell Hausfeld DP5810-Q) had an air supply rating of 25.4 CFM at 90 psi.

Instrumentation measuring air and liquid flow rates and pressures at various locations monitored the flow during the experiment as described in (G. Chahine et al., 2008; Wu et al., 2010).

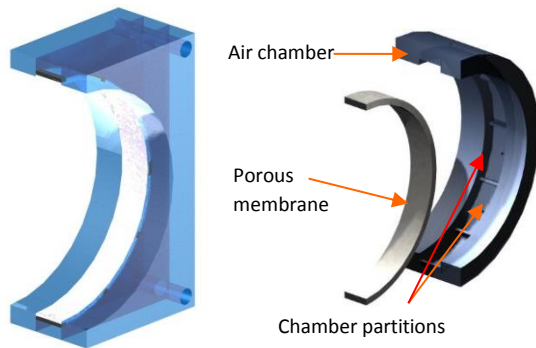


Figure 7: 3D rendering of the air injector positioned in the outer boundary of the half-3D nozzle. On the left is the injector assembly and on the right is an exploded view of the air chamber and porous membrane.

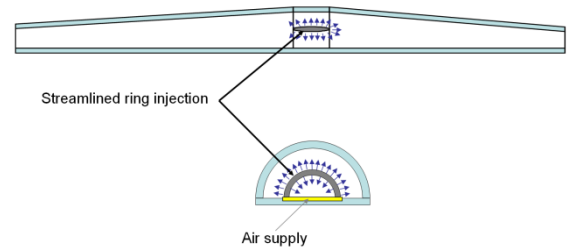


Figure 8: A sketch of the inner air injector of the half-3D nozzle.

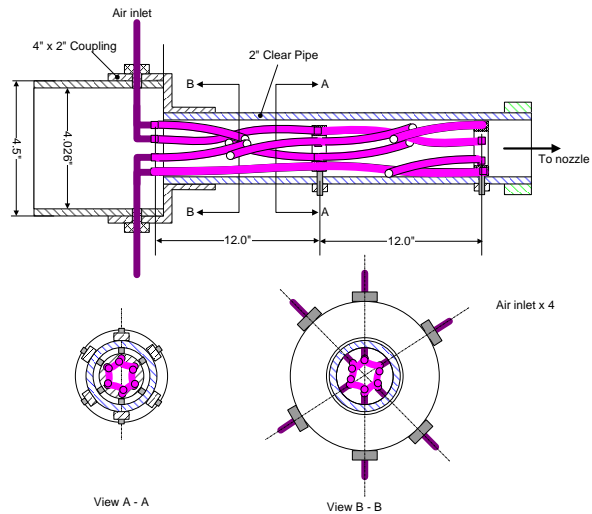


Figure 9: Air injection scheme for the convergent-divergent nozzles.

5.2 Thrust Measurement

To evaluate thrust augmentation an independent more direct technique to measure the thrust (in addition to the integrations in (4) and (5)) is desirable. In this study, this was evaluated by measuring directly the impact force on a large plate placed downstream of the nozzle exit and held rigidly against a force gauge. The force applied on the plate was measured by a load cell (PCB Load & Torque Model 1102-115-03A with full scale of 200 lbs force).

This force measurement is calibrated against the thrust measured using (5) to obtain a calibration factor, e . e is the ‘capture efficiency’ of the impact plate determined from liquid only tests as $F / \rho_{l,o} A_o u_{l,o}^2$, (the ratio of the captured exit force over the actual thrust). The ratio e varies with the size of the plate and standoff between nozzle and plate. These were selected to achieve an e as close to 1 as practical. This was defined and assessed in (Wu, Singh, et al., 2012; Choi, Wu, & Chahine, 2014). The thrust of the nozzle, T , is then determined from the force directly measured by the load cell, F , as:

$$T = \frac{F}{e} \quad (10)$$

For the results shown below, measuring the effects of the void fraction, α , on T involves comparative measurements and any errors on e are minimized in the process. Practically, this is a very efficient technique as one can in near real time observe the increase of T directly with the increase in α .

6 FLOW VISUALIZATION

6.1 Flow Inside the Divergent-Convergent Nozzle

An example of the bubbly flow along the convergent section of the half-3D nozzle can be seen in Figure 10. The nominal inlet velocity (averaged velocity computed as flow rate over the inlet area) was 3.57 m/s with the nominal void fraction (ratio of the flow rate of air over the flow rates of air plus water) of 16%. As shown in the figure, the bubble distribution in the convergent section is not uniform. It is clear that the void fraction at the top becomes higher as the flow moves towards the exit. This is caused by bubble rise to the top of the nozzle section due to buoyancy. This effect is much less prominent at higher liquid flow rates.

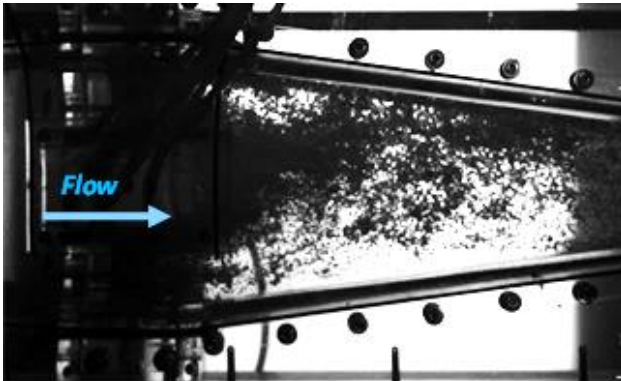


Figure 10: View of the contraction section of the half-3D BAP nozzle. Higher bubble concentration is observed at the top section as bubbles rise under gravity. Nominal inlet velocity is 3.57 m/s and nominal void fraction at the injection location is 16%.

6.2 Flow after the Divergent-Convergent Nozzle Exit

Flow visualizations showed clear large scale flow structures of the mixture once the two-phase medium exited the half-3D BAP nozzle.



Figure 11 shows an example of such flow structuring at the exit.

From previous studies (Wu, Singh, et al., 2012), it is found that the frequency of these structures increases with the flow rate and decreases with the void fraction. The corresponding Strouhal number,

$$S = \frac{fD}{u_0}, \quad (11)$$

where D is the nozzle exit diameter, and u_0 is the mean exit velocity, decreased with the void fraction regardless of the water flow rate.



Figure 11: Visualization of the large flow structures near the exit of the half-3D divergent-convergent nozzle. Nominal void fraction at injection location was $\alpha = 16\%$ and liquid flow rate was $0.87 \text{ m}^3/\text{min}$ (230 gpm).

6.3 Flow Inside the Convergent-Divergent Nozzle

In order to examine whether a shock or choked flow condition inside the convergent-divergent nozzle occur, high speed photography was used to visualize the flow through the circular convergent-divergent nozzle.

Figure 12 shows pictures of the divergent exit section of the nozzle at three different relatively low void fraction conditions, 0.2, 1.7, and 10%, with the liquid flow rate remaining at $0.38 \text{ m}^3/\text{min}$ (100 gpm). As seen in the

pictures, as the void fraction becomes higher, the bubbles appear to fill the nozzle section completely. Interestingly, at the highest void fraction, $\alpha = 10\%$ in the bottom picture, horizontal periodic clustering along the inside of the nozzle was observed, in which the bubbles group into vertical cloud layers inside the nozzle.

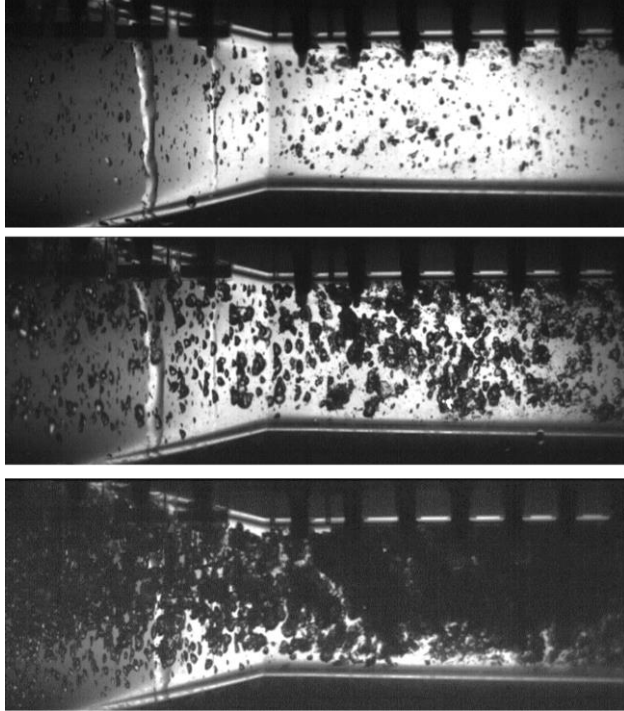


Figure 12: Visualization of the flow inside the circular convergent-divergent nozzle. Injection void fraction: (top) $\alpha = 0.2\%$, (middle) $\alpha = 1.7\%$, (bottom) $\alpha = 10\%$. Liquid flow rate was $0.38 \text{ m}^3/\text{min}$ (100 gpm) for all cases.

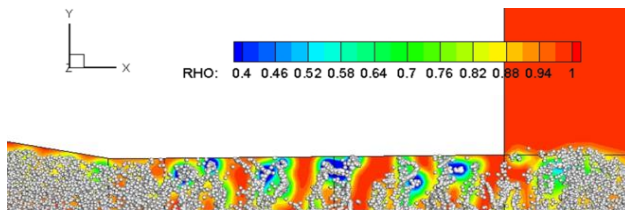


Figure 13: Simulation of the bubbly mixture flow in the convergent-divergent axisymmetric nozzle using 3DynaFS[®]. Water flow rate is $0.38 \text{ m}^3/\text{min}$ (100 gpm), initial bubble radius $400 \text{ }\mu\text{m}$, void fraction 10%.

Similar flow structures were observed in 3D simulations of the half-3D divergent-convergent nozzle (Choi et al., 2014). Figure 13 shows a simulated mixture flow in the nozzle for the injection void fraction of 10% with two way interactions. The 3D simulations shows also the structuring

into clusters in the divergent section. This is, however, much more prominent than in the experiment.

To better visualize the bubbly flow inside the nozzle the square convergent-divergent nozzle was used, with the jet exiting underwater or in air. Figure 14 shows pictures of the flow inside the square convergent-divergent nozzle at three different relatively low void fractions 3.6, 6.1, and 9.1% while the liquid flow rate remained at $0.38 \text{ m}^3/\text{min}$ (100 gpm). The pictures show irregular bubble clustering with no banding as in Figure 12. Additionally, no indication of choked flow can be observed at the throat or elsewhere in the nozzle.

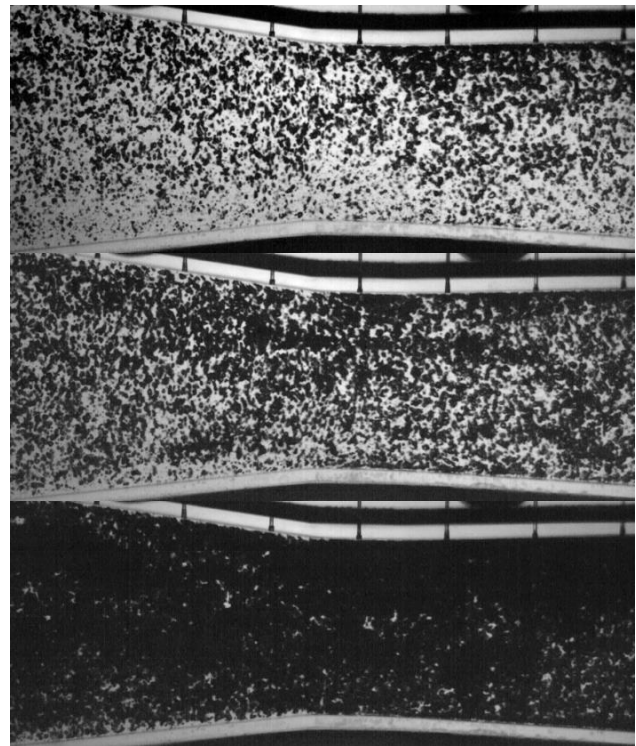


Figure 14: Visualization of the flow inside the square convergent-divergent nozzle without being submerged in water. Injection void fraction: (top) $\alpha = 3.6\%$, (middle) $\alpha = 6.1\%$, (bottom) $\alpha = 9.1\%$. Liquid flow rate was $0.38 \text{ m}^3/\text{min}$ (100 gpm) for all cases.

6.4 Flow After the Convergent-Divergent Nozzle Exit

Examples of the bubbly flow exiting from the square convergent-divergent nozzle are shown in Figure 15. The flow is very different from the bubbly flow downstream of the exit of the half-3D divergent-convergent nozzle, where strong periodic vortical flow structures were observed. No such structures can be observed here. At the lowest void

fraction in the top picture in Figure 15, small surface wave development can be observed.

At much higher void fraction, as shown in the bottom picture in Figure 15, strong wave structure growth of the jet shear layer can be observed. The expansion of the jet after the exit is significant and the strong oscillation of the jet diameter is prominent. However, regardless of the void fraction, no periodic vortex detachment can be observed in this case.

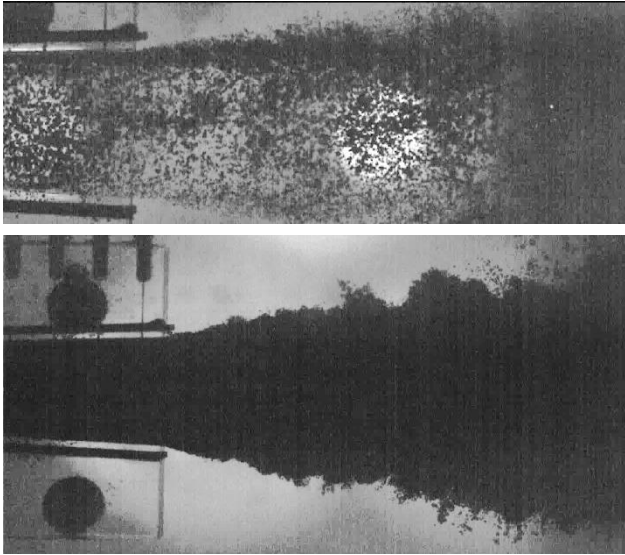


Figure 15: Visualization of the flow after the submerged square convergent-divergent nozzle exit at two different void fractions: (top) $\alpha = 3\%$ and (bottom) $\alpha = 66\%$ respectively. Liquid flow rate was $0.38 \text{ m}^3/\text{min}$ (100 gpm) for all cases.

7 POTENTIAL SUPERSONIC FLOW IDENTIFICATION

7.1 Pressure Profiles

Since evidence of a supersonic or choked flow was not readily available from flow visualization, extensive pressure measurements were conducted to obtain longitudinal pressure profiles in the circular convergent-divergent nozzle.

Figure 16 shows the axial locations of the pressure ports on the nozzle together with the port identification numbers. Port number 2 is at the beginning of the convergent section, and port number 14 is at the throat. Except for port numbers 14 and 15, at which only one pressure transducer was used, all other port locations had two pressure transducers separated by 90° in the circumferential direction to enable averaging the pressures measured in a given cross-section.

Figure 17 shows the measured pressure profiles for different void fractions with the liquid flow rate kept at $0.38 \text{ m}^3/\text{min}$ (100 gpm). As shown in the figure, the pressures increase with the increase in the void fraction (achieved by increasing the air injection flow rate). The pressure along the nozzle axis exhibits two different trends before and after the nozzle throat. In the convergent section upstream of the nozzle throat, the pressure decreases along the convergent section consistently. In the divergent section however, we observe a reversal of the pressure gradient. For low void fractions, as for a liquid only flow, the pressure, which reaches a minimum at the throat, increases along the divergent section to reach the ambient pressure at the nozzle exit. For the higher void fraction, the throat pressure is no longer a minimum and the pressure continues decreases as the liquid moves to the nozzle exit. The trend reversal is observed when the void fraction exceeds $\alpha = 0.15$. This pressure profile reversal is consistent with the expected behavior in a supersonic flow downstream of the throat. As shown in Figure 17 the dimensional pressures at the last port 13 before the exit increases with α , which is consistent with the behavior of a supersonic flow. Figure 18 shows the same pressure profiles as in Figure 17 normalized by the pressure difference between the inlet (port number 2) and the throat (port number 14), i.e. $(P - P_{14}) / (P_2 - P_{14})$. The trend reversal is illustrated better in the normalized pressure profiles. As shown in the figure, the pressure profiles along the convergent section collapse together quite well. However, in the divergent section, the slopes of the normalized pressure profile change significantly from positive to negative as the void fraction increases from $\alpha = 0$ to $\alpha = 0.32$.

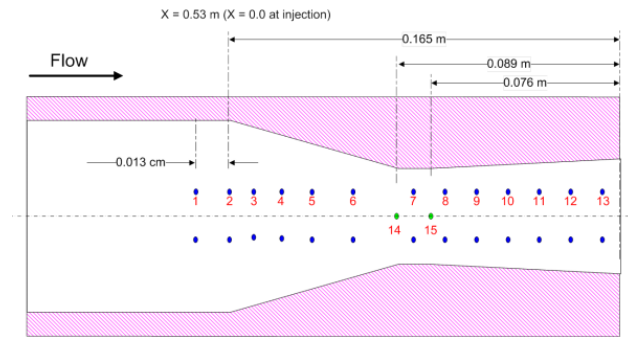


Figure 16: Sketch of the location of the pressure ports relative to the nozzle exit location and the beginning of the convergent section.

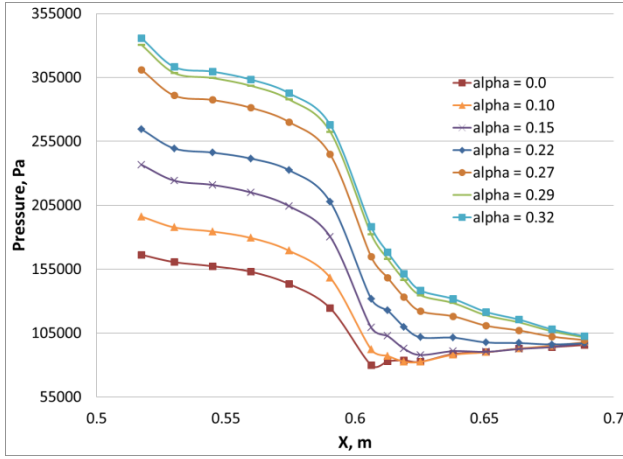


Figure 17: Pressure profile along the length of the nozzle for different void fractions at injection between 0 and 32%. The liquid flow rate is $0.38 \text{ m}^3/\text{min}$ (100 gpm).

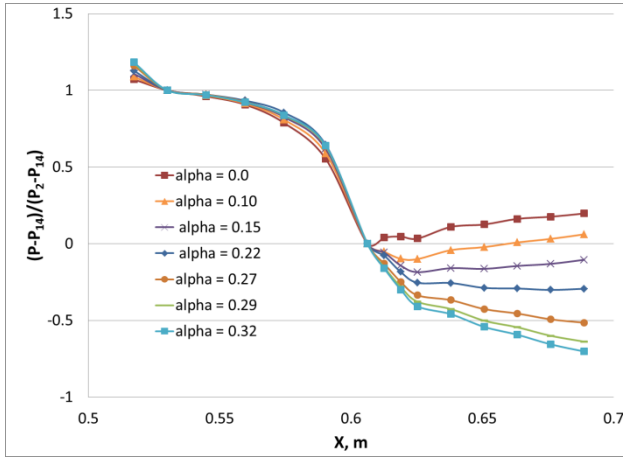


Figure 18: Pressure profiles shown in Figure 17 after normalizing with the pressure difference between the inlet and the throat, $(P - P_{14}) / (P_2 - P_{14})$. The liquid flow rate is $0.38 \text{ m}^3/\text{min}$ (100 gpm).

7.2 Comparison of Mixture Velocity and Sound Speed

Although the pressure profile in the divergent section exhibits the behavior of a supersonic flow, there is no obvious change in the flow structure seen in either the flow visualizations or in the pressure measurements that can be interpreted as a clear indication of the presence of a shock or choked flow. Here, we compare for evaluation, the average mixture flow velocity with the local sound speed to see if supersonic flow occurred. Using the available air injection and the pressure profile data, $P(x)$, and assuming that bubbles expand isothermally, the local air flow rate, $Q_a(x)$, at any location x , of the nozzle can be derived from

$$Q_a(x) = \frac{P_{inj} Q_{a_inj}}{P(x)}, \quad (12)$$

in which P_{inj} is the pressure of the mixture at the injection location and Q_{a_inj} is the corresponding air flow rate at injection. The local average void fraction at any axial location x can therefore be subsequently deduced from $Q_a(x)$ and the liquid flow rate Q_l as:

$$\alpha(x) = \frac{Q_a(x)}{Q_a(x) + Q_l}. \quad (13)$$

Figure 19 shows the average void fraction variations along the nozzle axis at different air injection conditions estimated from the measured pressures using (12) and (13) for a liquid flow rate of $0.38 \text{ m}^3/\text{min}$ (100 gpm). Overall, when the void fraction exceeds $\alpha = 0.15$, as in a choked flow, the void fraction increases monotonically along the nozzle axis regardless of the liquid flow rate. The sound speed can be estimated from the local void fraction using

$$\frac{1}{c^2} = [\rho_L(1-\alpha) + \rho_G\alpha] \left[\frac{\alpha}{kP} + \frac{(1-\alpha)}{\rho_L c_L^2} \right], \quad (14)$$

(Brennen, 1995) with the following values of the physical parameters: specific heat ratio $k = 1.0$, liquid density $\rho_L = 1000 \text{ kg/m}^3$, gas density $\rho_G = 1.2 \text{ kg/m}^3$, and sound speed in water $c_L = 1,485 \text{ m/s}$.

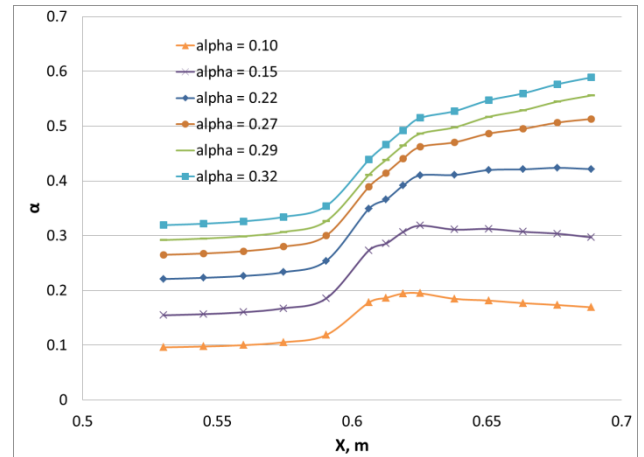


Figure 19: Average void fractions along the nozzle axis estimated from the pressure profiles shown in Figure 17 at different injection void fractions with a liquid flow rate of $0.38 \text{ m}^3/\text{min}$ (100 gpm).

The average mixture velocity, V_m , at any location, x , along the nozzle axis is estimated from the measured water and air flow rates, the deduced air flow rate at the location of

interest, and the corresponding area of the nozzle cross-section, A , as

$$V_m(x) = \frac{Q_l + Q_a(x)}{A(x)}. \quad (15)$$

Figure 20 shows comparisons of the deduced sound speeds and mixture velocities along the nozzle at different injection void fractions and at a liquid flow rate of $0.38 \text{ m}^3/\text{min}$ (100 gpm). Curves of the mixture sound speed and the mixture velocity intersect downstream of the throat section at a void fraction above $\sim 20\%$.

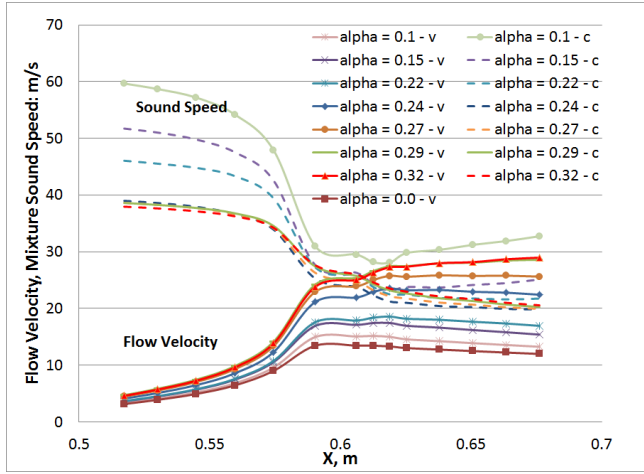


Figure 20: Variations of the sound speed and average mixture velocities deduced from the pressure measurements along the nozzle at different injection void fractions at liquid flow rate = $0.38 \text{ m}^3/\text{min}$ (100 gpm).

7.3 Two-Fluid Model

Since the occurrence of a choked flow condition is not clear, we consider below a two-fluid model to analyze the pressure profiles obtained from measurements. We assume subsonic conditions and apply Bernoulli equation to the flow along the nozzle, i.e.

$$2P_{inlet} + \rho V_{inlet}^2 = 2P(x) + \rho V^2(x), \quad (16)$$

From which we can deduce the velocity at location x :

$$V_x = \sqrt{2 \frac{P_{inlet} - P_x}{\rho} + V_{inlet}^2}. \quad (17)$$

Using the measured pressure profile along the nozzle axis, we obtain the air flow rate as in (12). From the definition of the void fraction, we can relate the pressures and void fractions at two locations, 1 and 2 by:

$$P_1 \alpha_1 = \frac{P_1 Q_{air1}}{Q_{air1} + Q_{liq}}, \quad P_2 \alpha_2 = \frac{P_2 Q_{air2}}{Q_{air2} + Q_{liq}}. \quad (18)$$

Therefore, the void fraction at location 2 can be calculated from that at location 1 using:

$$\alpha_2 = \frac{P_1 \alpha_1}{P_2} \frac{1}{\left(\alpha_1 \frac{P_1}{P_2} + (1 - \alpha_1) \right)}. \quad (19)$$

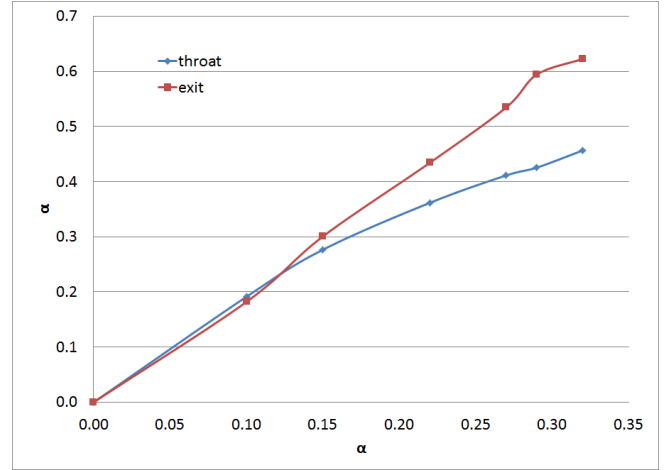


Figure 21: Variations of void fraction at throat, α_{throat} , and void fraction at exit, α_{exit} , with the inlet void fraction, α_{inlet} , at a liquid flow rate of $0.38 \text{ m}^3/\text{min}$ (100 gpm).

Using the conditions (liquid flow rate of $0.38 \text{ m}^3/\text{min}$ (100 gpm)) and pressure profile shown in Figure 17, the void fraction at the throat, α_{throat} , and void fraction at the exit, α_{exit} , can be calculated as functions of the inlet void fraction, α_{inlet} using (19). Figure 21 shows the variations of α_{throat} and α_{exit} with α_{inlet} . As the injection void fraction increases, the void fraction at the exit starts to surpass the void fraction at the throat, consistent with the pressure profile trend in the divergent section of the nozzle.

The velocities of the mixture at the throat and at the exit can then be calculated using (17). Figure 22 shows these as functions of the injection void fraction. The figure also shows the mixture sound speed at the throat and at the exit using the calculated α_{throat} and α_{exit} . This shows that the choked flow condition is not achieved at the throat in this case, but that supersonic flow condition could be achieved at the nozzle exit at void fractions higher than 27%.

Since the specific heat ratio may have a strong effect on the mixture sound speed calculation, the same calculations were repeated by assuming an adiabatic process with $k = 1.4$ while all other parameters remain the same. Figure 23 compares the mixture velocity and the mixture sound speed thus obtained at the nozzle throat and exit. In this case, the flow is still a subsonic even at the exit.

It is interesting to note that the two-fluid model indicates that for increasing α , the solution approaches a supersonic flow at the exit and not at the throat. This is due to the fact that, with bubble expansion and variation of α along x , the effective cross-section area of the nozzle (as predicted by this model) attains a minimum at the exit. In other words, upstream of the nozzle exit, the effective nozzle for the liquid is transformed into an almost purely convergent nozzle.

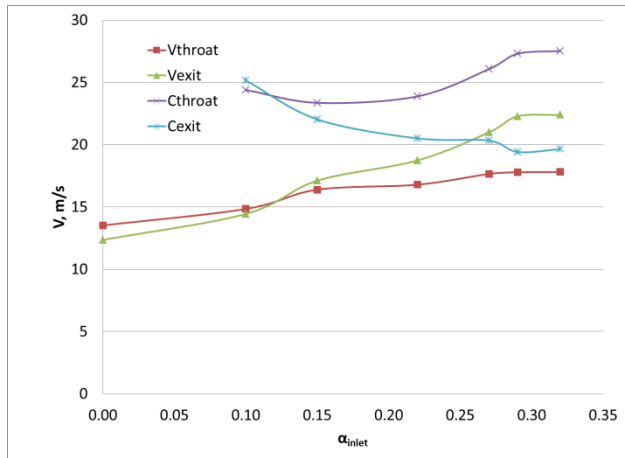


Figure 22: Variations of the sound speeds and average mixture velocities at nozzle throat and exit with injection void fractions at a liquid flow rate = $0.38 \text{ m}^3/\text{min}$ (100 gpm). $k = 1.0$, $\rho_L=1000 \text{ kg/m}^3$, $\rho_G= 1.2 \text{ kg/m}^3$, and $c_L=1485 \text{ m/s}$.

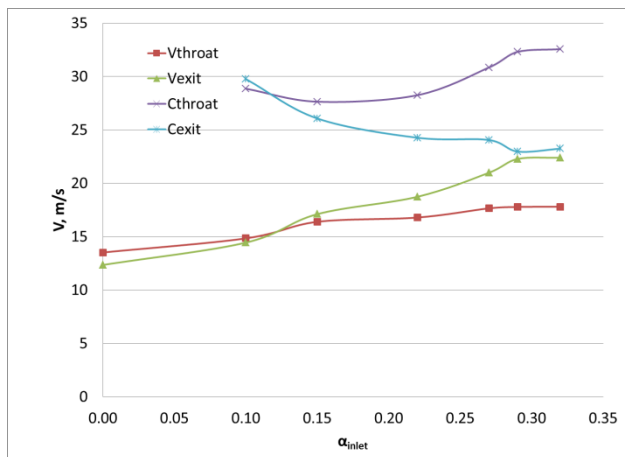


Figure 23: Variations of the sound speeds and average mixture velocities at nozzle throat and exit with injection void fractions at a liquid flow rate = $0.38 \text{ m}^3/\text{min}$ (100gpm). $k = 1.4$, $\rho_L=1000 \text{ kg/m}^3$, $\rho_G= 1.2 \text{ kg/m}^3$, and $c_L=1485 \text{ m/s}$.

8 THRUST AUGMENTATION

To measure the thrust of the convergent-divergent and divergent-convergent nozzles, the impact force measurement scheme described earlier was used for the half-3D divergent-convergent nozzle and the circular convergent-divergent nozzle. Figure 24 compares the waterjet thrust augmentation index, ζ_w , as defined in (7), as a function of the exit void fraction for the two types of nozzles.

The thrust measurements indicate that the overall relationship between ζ_w and α_{exit} for the convergent-divergent nozzle is similar to that of the half-3D divergent-convergent nozzle. In addition, the measured thrusts agree well with the thrust augmentation computations with the 1D numerical model. No sudden jump indicating improved performance because of shock formation can be observed within the range of experiments. This is contrary to the expectation that such a performance jump would occur as a result of the choked flow conditions. However, the performance of the circular convergent-divergent nozzle surpasses the performance of the half-3D divergent-convergent nozzle as the exit void fraction becomes larger. The waterjet thrust augmentation ζ_w of the circular convergent-divergent nozzle was about 20% higher than that achieved with the divergent-convergent nozzle for exit void fractions greater than 30%. This difference could be due to the fact that a supersonic regime may have been reached locally right at the exit instead of the throat as assumed in the calculations.

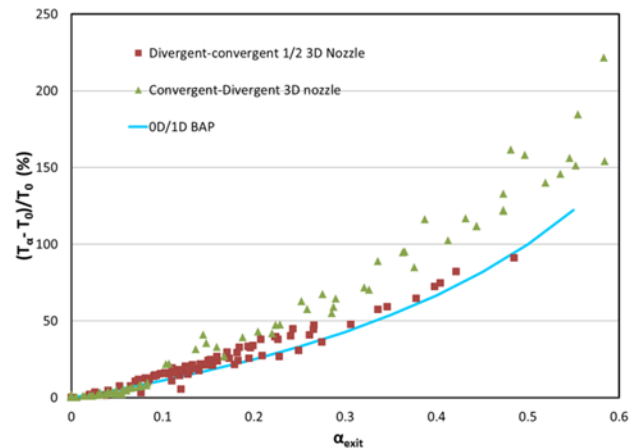


Figure 24: Normalized waterjet thrust augmentation, ζ_w , vs. exit void fraction.

9 CONCLUSIONS

Two nozzle configurations were designed and tested for their thrust performance with bubble injection: a divergent-convergent nozzle and a convergent-divergent nozzle.

Flow visualizations showed sometimes inhomogeneous bubble distributions inside the nozzles. However, the flow structure ejected from the nozzle exit are quite different. Distinct vortical structures were observed after the divergent-convergent nozzle exit, while only wavy structure development was observed from the jet exiting the convergent-divergent nozzle. Numerical simulation predicted the clustering of bubbles along the convergent-divergent nozzle axis but this effect was stronger than in the flow visualizations.

Identification of choked flow in the convergent-divergent nozzle remained inclusive. The flow visualization captured no distinct features indicating shock formation or choking for the convergent-divergent nozzle. However, the pressure profiles inside the convergent-divergent nozzle showed definite features usually associated with supersonic flows when the void fraction exceeded a threshold value. The pressure gradient in the exit divergent section of the nozzle became negative instead of positive as in water only flow conditions. No sudden pressure jump from the measured pressure profiles was observed downstream of the throat, and the liquid flow kept increasing beyond the supposed choking condition. Comparison of the local mixture sound speed and mixture velocity showed indications of a supersonic condition. The two-fluid model seemed to indicate no choking but instead a change in the effective nozzle cross section areas into a convergent only nozzle due to void fraction increase along the flow path.

The thrust was measured using the force felt by an impact plate. The experiments showed good nozzle performance with significant increase in the thrust with the air injection rate. A well-designed flow nozzle of either type could provide significant performance improvement, with a thrust increase index ξ_w of more than 160% at an exit void fraction of 60%. However, the thrust increase index was similar for both types of nozzles; the index for a convergent-divergent nozzle is about 20% higher than that for the divergent-convergent nozzle. Within the void fraction range covered by the experiments, the experimentally measured pressure profiles showed no sudden jump and the thrust increased in a continuous manner as the void fraction increased.

ACKNOWLEDGMENTS

This work was supported by the Office of Naval Research under contract N00014-11-C-0482 monitored by Dr. Ki-Han Kim. This support is very highly appreciated.

REFERENCES

Ahmed, W. H., Ching, C. Y., & Shoukri, M. (2007). Pressure recovery of two-phase flow across sudden expansions. *International Journal of Multiphase Flow*, 33(6), 575–594.

- Aloui, F., Doublicz, L., Legrand, J., & Souhar, M. (1999). Bubbly flow in an axisymmetric sudden expansion: Pressure drop, void fraction, wall shear stress, bubble velocities and sizes. *Experimental Thermal and Fluid Science*, 19(2), 118–130.
- Balakhrisna, T., Ghosh, S., Das, G., & Das, P. K. (2010). Oil–water flows through sudden contraction and expansion in a horizontal pipe – Phase distribution and pressure drop. *International Journal of Multiphase Flow*, 36(1), 13–24.
- Bertola, V. (2004). The structure of gas–liquid flow in a horizontal pipe with abrupt area contraction. *Experimental Thermal and Fluid Science*, 28(6), 505–512.
- Brennen, C. E. (1995, January 1). *Cavitation and Bubble Dynamics*. Oxford University Press.
- Chahine, G., Hsiao, C.-T., Choi, J.-K., & Wu, X. (2008). Bubble Augmented Waterjet Propulsion: Two-Phase Model Development and Experimental Validation. In *27th Symposium on Naval Hydrodynamics*. Seoul, Korea.
- Chahine, G. L. (2008). Numerical Simulation of Bubble Flow Interactions. In *Journal of Hydrodynamics* (Vol. 21, pp. 316–332). Warwick University, UK.
- Choi, J., Wu, X., & Chahine, G. L. (2014). Bubble Augmented Propulsion with a Convergent-Divergent Nozzle. In *Proc. 30th Symposium on Naval Hydrodynamics*. Hobart, Tasmania, Australia.
- Eskin, N., & Deniz, E. (2012). Pressure drop of two-phase flow through horizontal channel with smooth expansion. In *International Refrigeration and Air Conditioning Conference*.
- Gany, A., & Gofer, A. (2011). Study of a Novel Air Augmented Waterjet Boost Concept. In *Proc. 11th International Conference on Fast Sea Transportation FAST 2011*. Honolulu, Hawaii, USA.
- Ishii, R., Umeda, Y., Murata, S., & Shishido, N. (1993). Bubbly flows through a converging–diverging nozzle. *Physics of Fluids A: Fluid Dynamics*, 5(7), 1630.
- Johnson, V. E., & Hsieh, T. (1966). The Influence of the Trajectories of Gas Nuclei on Cavitation Inception. In *Proc. 6th Symposium on Naval Hydrodynamics*. (pp. 163–179).

- Kameda, M., & Matsumoto, Y. (1995). Structure of Shock Waves in a Liquid Containing Gas Bubbles. In *Proc. IUTAM Symposium on Waves in Liquid/Gas and Liquid/Vapor Two Phase Systems*.
- Kourakos, V. G., Rambbaud, P., Chabane, S., Pierrat, D., & Buchlin, J. M. (2009). Two-phase flow modelling within expansion and contraction singularities. In *Computational Methods in Multiphase Flow V*.
- Li, A., & Ahmadi, G. (1992). Dispersion and Deposition of Spherical Particles from Point Sources in a Turbulent Channel Flow. *Aerosol Science and Technology*, 16(4), 209–226.
- Mor, M., & Gany, A. (2004). Analysis of Two-Phase Homogeneous Bubbly Flows Including Friction and Mass Addition. *Journal of Fluids Engineering*, 126(1), 102.
- Muir, J. F., & Eichhorn, R. (1963). Compressible Flow of an Air-water Mixture Through a Vertical, Two-dimensional, Converging-diverging Nozzle. In *Proc. Heat Transfer and Fluid Mechanics Institute* (p. 32).
- Preston, A., Colonius, T., & Brennen, C. E. (2000). A Numerical Investigation of Unsteady Bubbly Cavitating Nozzle Flows. In *Proc. of the ASME Fluid Engineering Division Summer Meeting*. Boston, MA, USA.
- Saffman, P. G. (1965). The lift on a small sphere in a slow shear flow. *Journal of Fluid Mechanics*, 22(02), 385–400.
- Singh, S., Choi, J.-K. J., & Chahine, G. L. (2012). Optimum Configuration of an Expanding-Contracting-Nozzle for Thrust Enhancement by Bubble Injection. In *ASME Journal of Fluids Engineering* (Vol. 134, pp. 11302–11308). Vancouver, British Columbia, Canada.
- Singh, S., Fourmeau, T., Choi, J.-K., & Chahine, G. L. (2014). Thrust Enhancement through Bubble Injection Into an Expanding-Contracting-Nozzle with a Throat. In *2012 ASME International Mechanical Engineering Congress and Exposition* (Vol. 136, pp. 71301–71307). Houston, TX.
- Tangren, R. F., Dodge, C. H., & Seifert, H. S. (1949). Compressibility Effects in Two-Phase Flow. *Journal of Applied Physics*, 20(7), 637.
- Wang, Y.-C., & Brennen, C. E. (1999). Numerical Computation of Shock Waves in a Spherical Cloud of Cavitation Bubbles. *Journal of Fluids Engineering*.
- Wu, X., Choi, J.-K., Hsiao, C.-T., & Chahine, G. L. (2010). Bubble Augmented Waterjet Propulsion: Numerical and Experimental Studies. In *28th Symposium on Naval Hydrodynamics*. Pasadena, CA.
- Wu, X., Choi, J.-K., Singh, S., Hsiao, C.-T., & Chahine, G. L. (2012). Experimental and Numerical Investigation of Bubble Augmented Waterjet Propulsion. *Journal of Hydrodynamics*, 24(5), 635–647.
- Wu, X., Singh, S., Choi, J.-K., & Chahine, G. L. (2012). Waterjet Thrust Augmentation using High Void Fraction Air Injection. In *29th Symposium on Naval Hydrodynamics*. Gotheburg, Sweden.